






Terahertz photodetection in scalable single-layer-graphene and hexagonal boron nitride heterostructures

Cite as: Appl. Phys. Lett. **121**, 031103 (2022); doi: 10.1063/5.0097726

Submitted: 1 May 2022 · Accepted: 17 June 2022 ·

Published Online: 19 July 2022



M. Asgari,¹ L. Viti,¹  O. Balci,² S. M. Shinde,² J. Zhang,² H. Ramezani,² S. Sharma,² A. Meersha,² G. Menichetti,³  C. McAleese,⁴ B. Conran,⁴ X. Wang,⁴  A. Tomadin,³ A. C. Ferrari,²  and M. S. Vitiello^{1,a)} 

AFFILIATIONS

¹NEST, CNR-Istituto Nanoscienze and Scuola Normale Superiore, Piazza San Silvestro 12, Pisa 56127, Italy

²Cambridge Graphene Centre, University of Cambridge, Cambridge CB3 0FA, United Kingdom

³Dipartimento di Fisica, Università di Pisa, Largo Bruno Pontecorvo 3, 56127 Pisa, Italy

⁴AIXTRON Ltd., Buckingham Business Park Anderson Rd., Swavesey, Cambridge CB24 4FQ, United Kingdom

Note: This paper is part of the APL Special Collection on Photodetectors Based on Van der Waals Heterostructures and Hybrid 2D Materials.

^{a)} Author to whom correspondence should be addressed: miriam.vitiello@sns.it

ABSTRACT

The unique optoelectronic properties of single layer graphene (SLG) are ideal for the development of photonic devices across a broad range of frequencies from x rays to microwaves. In the terahertz (THz) frequency range (0.1–10 THz), this has led to the development of optical modulators, nonlinear sources, and photodetectors with state-of-the-art performances. A key challenge is the integration of SLG-based active elements with pre-existing technological platforms in a scalable way, while maintaining performance level unperturbed. Here, we report room temperature THz detectors made of large-area SLG, grown by chemical vapor deposition (CVD) and integrated in antenna-coupled field effect transistors. We selectively activate the photo-thermoelectric detection dynamics, and we employ different dielectric configurations of SLG on Al₂O₃ with and without large-area CVD hexagonal boron nitride capping to investigate their effect on SLG thermoelectric properties underpinning photodetection. With these scalable architectures, response times ~ 5 ns and noise equivalent powers (NEPs) ~ 1 nW Hz^{-1/2} are achieved under zero-bias operation. This shows the feasibility of scalable, large-area, layered material heterostructures for THz detection.

© 2022 Author(s). All article content, except where otherwise noted, is licensed under a Creative Commons Attribution (CC BY) license (<http://creativecommons.org/licenses/by/4.0/>). <https://doi.org/10.1063/5.0097726>

Layered materials (LMs) and related heterostructures (LMHs) are a versatile platform for engineering optoelectronic and photonic devices.^{1–3} They can be synthesized with wafer-scale methods^{2,4,5} and stacked to form LMHs. Being compatible with Si and a wider range of III–V materials and substrates,^{2,5–7} they open new prospects for emerging research domains, such as future high-density optical communications,⁶ high-speed datacom,⁸ quantum nanophotonics,⁹ and optoelectronics.^{1,3} In particular, LMs are a versatile platform for photodetectors (PDs) operating across a broad range of frequencies from microwaves¹⁰ to telecom,⁸ visible,^{1–3} and x rays.¹¹

Terahertz (THz) radiation (0.1–10 THz) finds application in biomedicine,¹² security,¹³ spectroscopy,¹⁴ cultural heritage,¹⁵ astronomy,¹⁶ real-time imaging,¹⁷ and high data-rate communications.¹⁸ In this

frequency range, optoelectronic systems employing LMs realized in scalable processes have mostly been developed for light modulation^{19,20} and nonlinear optics,^{21,22} whereas similar processes for nanoscale receivers are still at an early stage and limited to few examples involving scalable large-area single layer graphene (SLG).^{23–28}

The challenge is twofold. 1) The quest for technological maturity requires integration with established platforms, such as complementary metal oxide semiconductors (CMOSs). 2) Performance in SLG grown by chemical vapor deposition (CVD)^{24–28} still does not match that obtained with exfoliated hexagonal boron nitride (hBN)/SLG/hBN heterostructures.^{29–34} Above 1 THz, few ns response times (τ) and noise equivalent power (NEP) ~ 1 nW Hz^{-1/2} have been reported at room temperature (RT) on THz PDs based on large-area (\sim cm²)

TABLE I. Performance of room-temperature THz detectors based on scalable, large-area graphene.

Material	Frequency range (THz)	NEP ($\text{nW Hz}^{-1/2}$)	Response time (ns)
Epitaxial graphene on SiC ²³	0.2–0.4	80	n.a.
CVD graphene ²⁴	0.36	10	n.a.
CVD graphene ²⁵	0.4	0.13	n.a.
CVD graphene ²⁶	0.6	~0.5	n.a.
CVD graphene ²⁷	~2	~150	n.a.
CVD graphene ²⁸	~3	~1 (Mean 4.3)	~5
CVD graphene, CVD hBN heterostructure	~3	~1 (Mean 3.0)	~7

CVD SLG,²⁸ but these are still inferior to those reported in high-quality hBN-encapsulated SLG ($\tau = 880$ ps, $\text{NEP} = 80 \text{ pW Hz}^{-1/2}$),^{29,31} in Schottky diodes³⁵ ($\text{NEP} \sim 100 \text{ pW Hz}^{-1/2}$, electrical bandwidth ~ 40 GHz, operation frequency < 1.8 THz), in high-electron-mobility transistors³⁶ (HEMTs, $\text{NEP} \sim 100 \text{ pW Hz}^{-1/2}$, $\tau < 10$ ps), or in portable THz cameras based on FETs or microbolometer arrays^{37,38} ($\text{NEP} \sim 30 \text{ pW Hz}^{-1/2}$, $\tau > 10 \mu\text{s}$). Table I summarizes the performance of RT THz detectors realized with scalable graphene-based structures.

As a step toward commercial development of THz PDs based on LMs and LMHs, we propose here the use of substrate treatment³⁹ or large-area encapsulation⁴⁰ to reach stable and repeatable state-of-the-art performances at RT. We develop RT PDs operating at 2.8 THz based on large-area ($\sim 1 \times 1 \text{ cm}^2$) CVD SLG with and without large-area ($\sim 1 \times 1 \text{ cm}^2$) CVD hBN capping, Fig. 1(a).

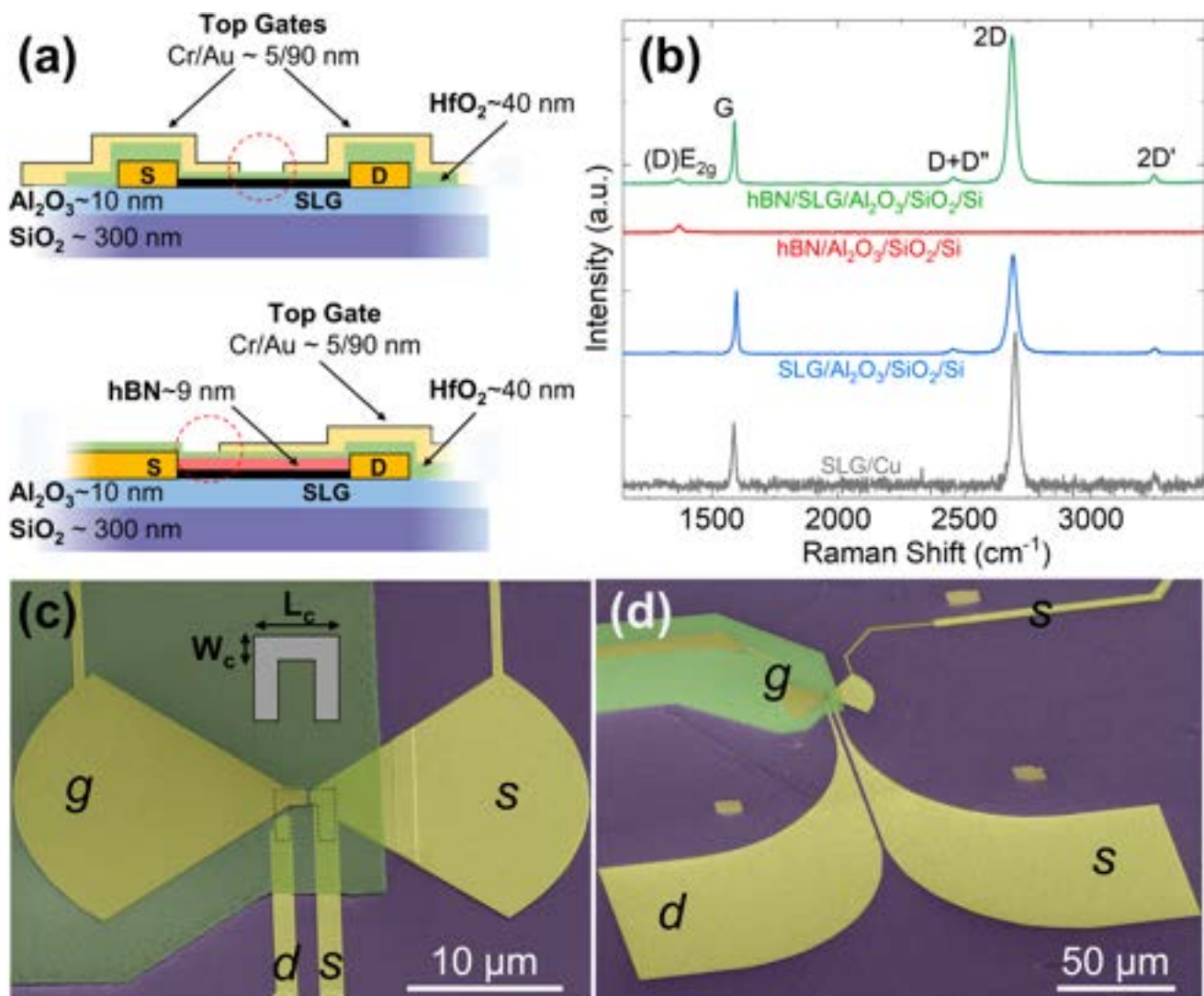


FIG. 1. (a) Schematic cross section of GFETs. Top: double-gated $\text{Al}_2\text{O}_3/\text{SLG}/\text{HfO}_2$. Bottom: single-gated $\text{Al}_2\text{O}_3/\text{SLG}/\text{hBN}/\text{HfO}_2$. Dashed red circles indicate the position of the THz-induced field enhancement. (b) Raman spectra of as-grown SLG on Cu and SLG transferred on Al_2O_3 with and without hBN capping. (c) and (d) False color scanning electron micrographs of a single-gated device. The inset shows the U-shaped channel.

A ~ 10 nm thick layer of Al_2O_3 is deposited on a SiO_2/Si substrate (resistivity ~ 10 k Ω cm) by atomic layer deposition (ALD) (see the [supplementary material](#)). SLG is grown in a hot wall CVD system using a ~ 30 μm thick Cu foil as a substrate. The foil, suspended on a quartz holder and loaded into the CVD system, is annealed at 1050°C for 2 h under H_2 gas (100 sccm) at 760 Torr and cooled down to RT. For the growth, the foil is annealed at 1050°C with 50 sccm hydrogen flow at 0.4 Torr for 2 h. 5 sccm CH_4 is introduced to start growth, which is completed in 30 min by stopping the CH_4 flow. The system is then naturally cooled down to RT under 50 sccm H_2 . As-grown SLG/Cu is spin-coated with poly (methyl methacrylate) (PMMA) (A4-950) at 1000 rpm for 1 min and baked at 80°C for 10 min. PMMA-coated SLG/Cu is kept in water overnight to oxidize the Cu foil. PMMA/SLG is then electrochemically delaminated by applying 2 V between the Pt anode and PMMA/SLG/Cu cathode in a NaOH aqueous electrolyte (~ 1 M). The PMMA/SLG stack is cleaned in water and transferred on $\text{Al}_2\text{O}_3/\text{SiO}_2/\text{Si}$ substrates, which are then baked at 80°C for 10 min after ~ 10 h natural drying. PMMA is removed by soaking in acetone and isopropyl alcohol (IPA).

hBN is grown on *c*-plane Al_2O_3 (0001) at 1400°C , 500 mbar for 30 min in an AIXTRON CCS 2D reactor. 10 sccm N_2 is used to transport the single-source precursor, borazine, to the reactor. Before hBN growth, the sapphire substrates are annealed in H_2 for 5 min at 750 mbar and 1180°C . As-grown hBN on *c*-plane sapphire is then spin-coated with PMMA (A4-950) at 1000 rpm for 1 min and baked at 80°C for 10 min. PMMA-coated hBN on sapphire is kept in $\sim 8\%$ H_3PO_4 for ~ 10 h to delaminate PMMA/hBN. This is cleaned in water and transferred on SLG/ $\text{Al}_2\text{O}_3/\text{SiO}_2/\text{Si}$. After natural drying, this is baked at 80°C for 10 min. PMMA is removed by soaking it in acetone and IPA.

As-grown and transferred SLG and hBN are characterized by Raman spectroscopy with a Renishaw InVia spectrometer equipped with $100\times$ objective at 514.5 nm. A statistical analysis of seven spectra on as-grown SLG on Cu, 27 spectra on SLG on $\text{Al}_2\text{O}_3/\text{SiO}_2/\text{Si}$, 36 spectra on hBN/ $\text{Al}_2\text{O}_3/\text{SiO}_2/\text{Si}$, and 26 spectra on hBN/SLG/ $\text{Al}_2\text{O}_3/\text{SiO}_2/\text{Si}$ is performed to estimate the defect density and doping. Errors are calculated from the standard deviation across different spectra, the spectrometer resolution (~ 1 cm^{-1}), and the uncertainty associated with different methods to estimate doping from the position of G peak Pos(G), its full-width-half-maximum [FWHM(G)], the intensity and area ratios I(2D)/I(G), A(2D)/A(G), and the position of 2D peak Pos(2D).^{41–43} The Raman spectrum of as-grown SLG on Cu is in [Fig. 1\(b\)](#), after Cu photoluminescence removal.⁴⁴ The 2D peak is a single Lorentzian with $\text{FWHM}(2\text{D}) = 30 \pm 5$ cm^{-1} , which is a signature of SLG.⁴⁵ Pos(G) = 1584 ± 2 cm^{-1} , $\text{FWHM}(G) = 16 \pm 4$ cm^{-1} , Pos(2D) = 2698 ± 2 cm^{-1} , and $I(2\text{D})/I(G) = 3.8 \pm 1.0$ $A(2\text{D})/A(G) = 7.2 \pm 1.8$. No D peak is observed, indicating negligible density of Raman active defects.^{46,47} A typical Raman spectrum of SLG/ $\text{Al}_2\text{O}_3/\text{SiO}_2/\text{Si}$ is in [Fig. 1\(b\)](#). The 2D peak retains its single-Lorentzian line shape with $\text{FWHM}(2\text{D}) = 36 \pm 2$ cm^{-1} . Pos(G) = 1597 ± 3 cm^{-1} , $\text{FWHM}(G) = 14 \pm 2$ cm^{-1} , Pos(2D) = 2692 ± 2 cm^{-1} , $I(2\text{D})/I(G) = 1.9 \pm 0.5$, and $A(2\text{D})/A(G) = 4.9 \pm 0.5$, indicating a p-doping with Fermi level $E_F = 290 \pm 90$ meV,^{41,42} which corresponds to a carrier concentration $n = 6.5 \pm 3.3 \times 10^{12}$ cm^{-2} .^{41,42} $I(D)/I(G) = 0.03 \pm 0.04$ corresponds to a defect density $n_D = 1.7 \pm 0.7 \times 10^{10}$ cm^{-2} for excitation energy 2.41 eV and $E_F = 290 \pm 90$ meV.⁴³ A Raman spectrum of the transferred hBN on $\text{Al}_2\text{O}_3/\text{SiO}_2/\text{Si}$ is in [Fig. 1\(b\)](#). The position of E_{2g} peak is

$\text{Pos}(E_{2g}) = 1371 \pm 1$ cm^{-1} , with $\text{FWHM}(E_{2g}) = 26 \pm 1$ cm^{-1} .⁴⁸ A Raman spectrum of SLG capped by hBN is in [Fig. 1\(b\)](#). The single-Lorentzian 2D peak has $\text{FWHM}(2\text{D}) = 37 \pm 2$ cm^{-1} . Pos(G) = 1598 ± 3 cm^{-1} , $\text{FWHM}(G) = 13 \pm 1$ cm^{-1} , Pos(2D) = 2692 ± 2 cm^{-1} , $I(2\text{D})/I(G) = 1.8 \pm 0.3$, and $A(2\text{D})/A(G) = 5.1 \pm 0.6$, indicating a p-doping with $E_F = 300 \pm 100$ meV,^{41,42} which corresponds to $n = 7.2 \pm 4.1 \times 10^{12}$ cm^{-2} .^{41,42}

Graphene field-effect transistors (GFETs) are fabricated by electron beam lithography (EBL) (Zeiss UltraPlus), ALD (Oxford, OpAL), and metal evaporation. We define U-shaped channels with length $L_c = 2400$ nm and width $W_c = 1500$ nm through reactive ion etching (O_2 for uncapped, CF_4/O_2 mixture for hBN-capped samples). We pattern source (*s*) and drain (*d*) contacts via EBL, and fabrication is finalized by depositing a 40 nm thick Pd layer by thermal evaporation and liftoff. For hBN-capped devices, this results in edge-contacts to the SLG channel, showing contact resistance $R_0 \sim 1$ k Ω similar to the case of uncapped samples. We then define the top-gate oxide (~ 40 nm HfO_2 , grown by ALD) above the channel and finalize the fabrication by depositing 5/90 nm Cr/Au to establish the top-gate (*g*) electrodes. To reduce the detector shunt capacitance, *s* and *d* electrodes are connected to a coplanar strip line.³¹ A schematic cross section of the fabricated devices is in [Fig. 1\(a\)](#). For each material combination, $\text{Al}_2\text{O}_3/\text{SLG}/\text{HfO}_2$ and $\text{Al}_2\text{O}_3/\text{SLG}/\text{hBN}/\text{HfO}_2$, two distinct architectures are conceived, devised, and investigated. The first is based on single-top-gated GFETs integrated with a planar bow-tie antenna with radius 24 μm and flare angle 90° [[Figs. 1\(c\)](#) and [1\(d\)](#)]. The antenna arms are connected to the *s* and *g* electrodes. The second design features two top-gates, connected to the left and right arms of a 24 μm radius bow-tie antenna. The antenna dimensions are chosen to be resonant with a radiation frequency of 2.8 THz.²⁸

These geometries are selected to activate the photo-thermoelectric (PTE) effect as a dominant detection mechanism.^{31,32,49} This requires a spatial asymmetry along the source-drain (*s-d*) channel.³ In single-gated systems, the asymmetry is established by the spatial gradient of the electronic temperature (T_e) in the SLG channel, induced by the absorption of THz light in the antenna gap, which is located close to the *s* electrode.³¹ Instead, in *p-n* junctions, the electronic distribution is symmetrically heated at the center of the *s-d* channel, where the antenna gap is located.²⁹ Here, the asymmetry is determined by the longitudinal variation of the SLG Seebeck coefficient (S_b), whose profile along the *s-d* direction can be electrostatically defined by applying distinct gate voltages (V_g) on the left and right sides of the junction.

We activate a dominant PTE by design, since SLG displays unique thermoelectric properties, due to its low electronic specific heat (~ 2000 $k_B \mu\text{m}^{-2}$ at RT,⁵⁰ where k_B is the Boltzmann constant), ultrafast (~ 30 fs) carrier thermalization dynamics,⁵¹ and slower (~ 4 ps) electron-phonon cooling.^{52,53} Thus, it offers an outstanding route for performance optimization by means of, e.g., carrier lifetime engineering⁴⁹ or coupling to plasmonic-polaritonic quasi-particles.⁵⁴ PTE also allows for broadband,⁴⁹ RT, zero-bias operation.⁸

We first characterize the devices electrically by measuring the source-drain current (I_{sd}) as a function of V_g . The resistance (*R*) curve for a single-gated device is in [Fig. 2\(a\)](#). Instead, [Fig. 2\(b\)](#) shows the resistance map of a *p-n* junction device, measured as a function of the left- and right-gate voltages (V_{gL} and V_{gR}). We extract the field-effect mobility (μ_{FE}) for electrons and holes and the residual carrier density

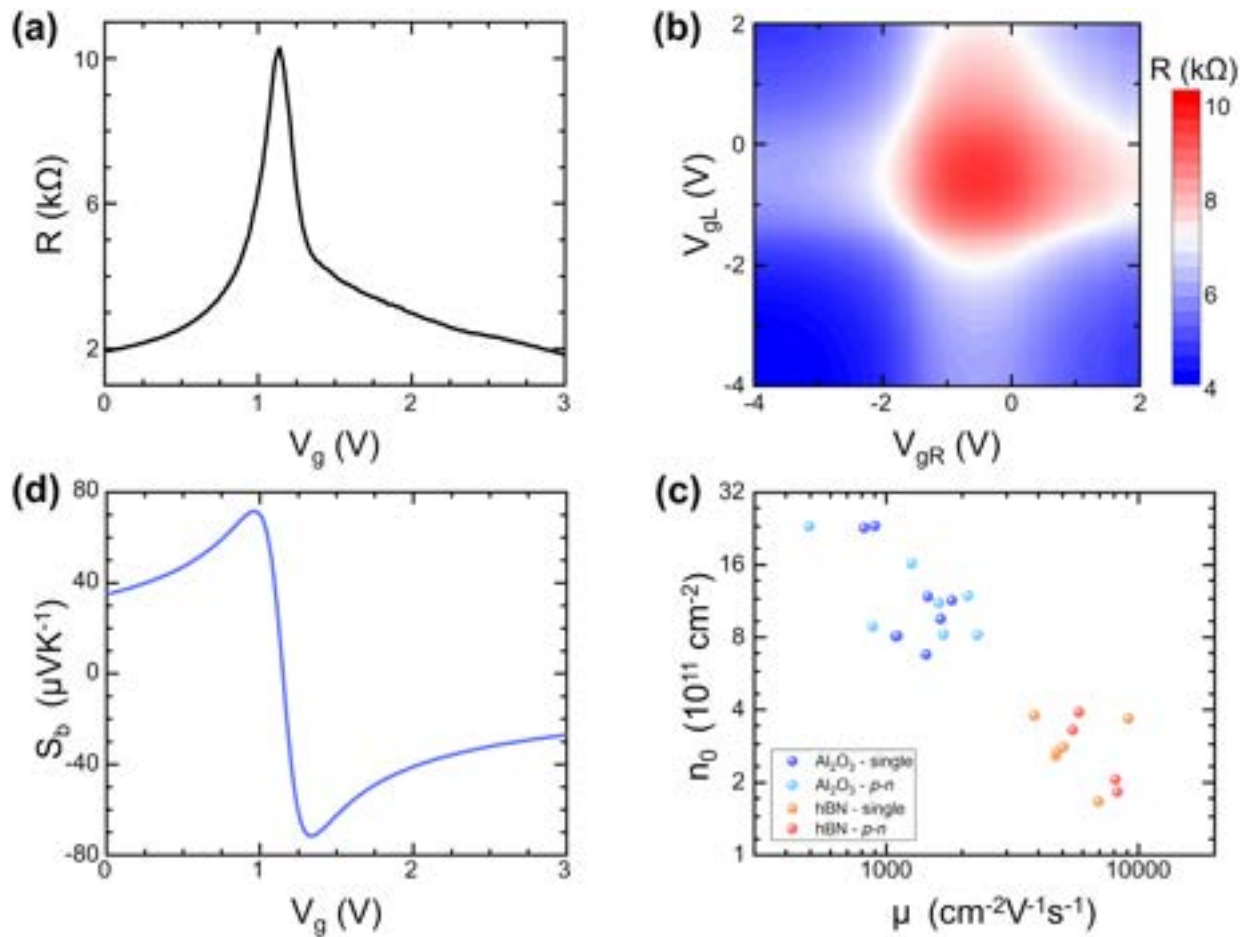


FIG. 2. (a) Channel resistance vs V_g for an hBN-capped, single-gated GFET. (b) Map of R as a function of V_{gR} and V_{gL} for an hBN-capped p - n junction. (c) Chart of n_0 vs μ_{FE} for all the measured devices. Blue (light-blue) dots represent single-gated (double-gated) FETs without hBN-capping. Orange (red) dots represent hBN-capped single-gated (double-gated) FETs. (d) S_b calculated with the Boltzmann EMT^{51,56,57} for the R curve in (a).

(n_0) by using the fitting function⁵⁵ $R = R_0 + (L_c/W_c) \cdot (1/n_{2d}e\mu_{FE})$, where $n_{2d} = \{n_0^2 + [C_g/e \cdot (V_g - V_{CNP})]^2\}^{-1/2}$ is the carrier density,⁵⁵ C_g is the gate-capacitance per unit area, and V_{CNP} is the charge neutrality point. We get $\mu_{FE} = 300$ – $2000 \text{ cm}^2 \text{ V}^{-1} \text{ s}^{-1}$ for $\text{Al}_2\text{O}_3/\text{SLG}$ -based GFETs and $\mu_{FE} = 3000$ – $9000 \text{ cm}^2 \text{ V}^{-1} \text{ s}^{-1}$ for hBN-capped ones.

Figure 2(c) plots n_0 as a function of μ for the complete batch of devices, where μ is the average field-effect mobility of electrons and holes: each GFET is represented by a colored dot. From this comparison, hBN-capped samples show lower n_0 and higher μ with respect to $\text{Al}_2\text{O}_3/\text{SLG}/\text{HfO}_2$ devices. The field-effect measurements [Figs. 2(a) and 2(b)] can be used to evaluate S_b , which determines the PTE response of SLG-based PDs. This can be done starting from the experimental conductivity (σ) and using the Mott equation,³⁰ which, however, is not accurate at low carrier densities,⁵⁶ i.e., close to V_{CNP} . Thus, we theoretically calculate S_b using an effective medium theory (EMT)⁵⁶ in the framework of the linear Boltzmann equation^{53,57} (see the supplementary material). Figure 2(d) shows the results of the EMT

model applied to the device of Fig. 2(a), for which we get a maximum thermopower of $S_{\max} \sim 70 \mu\text{V K}^{-1}$.

We then evaluate the PDs' optical figures of merit: voltage responsivity (R_v), NEP, and τ . The detectors are illuminated by a 2.8 THz quantum cascade laser (QCL), driven in a pulsed mode (repetition rate 40 kHz, duty cycle 4%) delivering a peak power $\sim 25 \text{ mW}$, corresponding to an average power $\sim 1 \text{ mW}$. The antenna axis is oriented parallel to the linearly polarized electric field. The beam is focused by two TPX lenses onto a $\sim 200 \mu\text{m}$ radius circular spot. We select intermediate average power $P_0 = 0.4 \text{ mW}$ to characterize the PDs to avoid QCL overheating. The corresponding average intensity in the focal point is $I_0 = 0.32 \text{ W cm}^{-2}$.

We measure the photovoltage (Δu) at the d electrode, while keeping s grounded. Δu is amplified by a voltage preamplifier (DL Instruments, M1201, gain $\gamma = 1000$) and sent to a lock-in (Stanford Research, 5210). We use a square-wave envelope with frequency $f_{\text{mod}} = 1.333 \text{ kHz}$ as a lock-in reference and as a triggering signal for the QCL pulse trains. Δu can be inferred from the demodulated lock-in

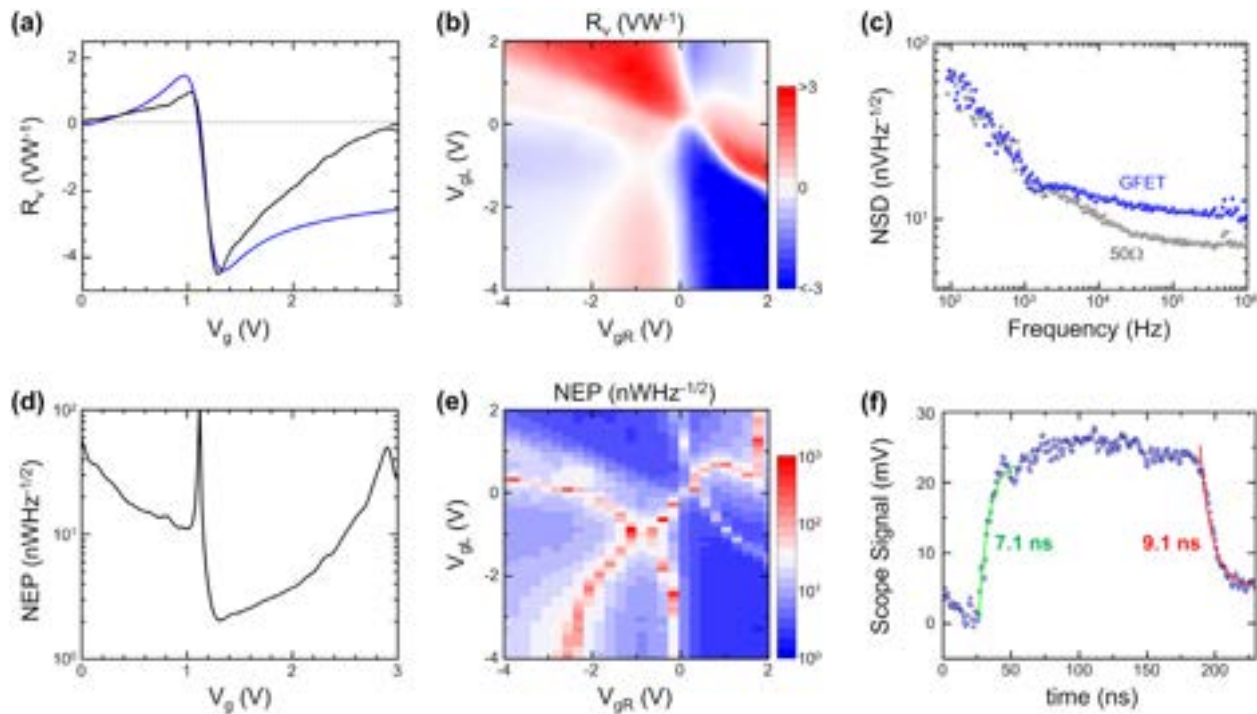


FIG. 3. (a) R_v as a function of V_g for an hBN-capped single-gated GFET. The experimental curve (black line) is compared with the theoretical PTE response (blue line), evaluated by EMT. (b) R_v map of an hBN-capped p - n junction as a function of V_{gL} and V_{gR} . (c) NSD of a GFET and of a $50\ \Omega$ resistor, measured by sweeping the reference frequency of the lock-in from 100 Hz to 1 MHz. (d) and (e) NEP of single-gated and p - n junction GFETs as a function of the gate voltage(s). (f) Time trace of an intensity fluctuation of the QCL. The rising and falling edges are fitted with exponential functions to retrieve τ .

signal (V_{LI}) as³⁰ $\Delta u = (\pi\sqrt{2}/2)V_{LI}/\gamma$, where the pre-factor $\pi\sqrt{2}/2$ takes into account that the lock-in measures the root mean square of the fundamental Fourier component of the square wave produced by the QCL modulation. R_v is calculated from the ratio between Δu and the power $P_a = I_0 A_{\text{eff}}$ impinging on the detector, with A_{eff} the detector effective area, assumed equal to the diffraction limited area³⁰ $A_{\text{eff}} = \lambda^2/4 = 2800\ \mu\text{m}^2$, where λ is the free-space wavelength. We calculate the curve of R_v vs V_g for each single-gated GFET and the map of R_v vs V_{gL} and V_{gR} for each p - n junction. Typical examples of R_v vs V_g plots are in Figs. 3(a) and 3(b) for a single-gated GFET and a p - n junction, respectively. The photoresponse in single-gated GFETs follows the profile of S_b with an offset of $S_{bu} \sim S_b$ ($V_g = 0$ V) and with PTE voltage³⁰ $V_{\text{PTE}} = \Delta T_e (S_b - S_{bu})$, where ΔT_e is the T_e gradient between s (hot) and d (cold) sides of the SLG channel and S_{bu} is the Seebeck coefficient of the ungated region between the s and g electrodes. Figure 3(a) compares the measured R_v vs V_g and the theoretical PTE responsivity, R_{PTE} , vs V_g , with R_{PTE} inferred from V_{PTE} by considering $\Delta T_e/P_0 \sim 1.5\ \text{K}/\text{mW}$, showing good qualitative agreement between the two curves. The discrepancy between theoretical and experimental responsivities at large positive V_g is ascribed to the fact that the adopted theoretical model (see the supplementary material) only includes electron scattering with charged Coulomb impurities as dominant effect limiting the conductivity, possibly neglecting additional contributions, e.g., phonon scattering or carrier inhomogeneities at the contacts. A dominant PTE detection mechanism is also observed in p - n junctions. E_F in SLG can be tuned

across the Dirac point by the electrostatic gating applied to the left and right sides of the junction. The nonmonotonic dependence of S_b on E_F leads to multiple sign changes in a sixfold pattern²⁹ in the R_v map [Fig. 3(b)], a distinctive feature of PTE.^{26,29}

The sensitivity of THz detectors is evaluated through the NEP,²⁹ defined as the ratio between noise figure and responsivity. In order to calculate NEP, it is important to give a rigorous evaluation of the noise spectral density (NSD).^{26,29-31} Thus, we measure the GFET NSD with a lock-in amplifier (Zurich Inst., UHFLI). The electrode is grounded and the signal, demodulated by the lock-in, is collected at the d electrode, while a sweep of the modulation frequency is performed. The results are in Fig. 4(c) for a $50\ \Omega$ test resistor and for a prototypical SLG-based device. The white noise floor for the $50\ \Omega$ resistor is dominated by the lock-in noise figure. The Johnson-Nyquist NSD formula gives³⁰ $N_j = (4k_B TR)^{-1/2} = 0.91\ \text{nV}\ \text{Hz}^{-1/2}$ for a $50\ \Omega$ resistor operated at RT, whereas our instrumental noise floor is $\sim 8\ \text{nV}\ \text{Hz}^{-1/2}$, as expected for the noise level of the employed lock-in.⁵⁸ The NSD of one of the GFETs [$R = 9\ \text{k}\Omega$ in Fig. 4(c)] is dominated by the $1/f$ component⁵⁹ for modulation frequency $< 1\ \text{kHz}$ and flattens at NSD $< 14\ \text{nV}\ \text{Hz}^{-1/2}$ at higher frequencies in agreement with the theoretically expected $N_j = 12.3\ \text{nV}\ \text{Hz}^{-1/2}$. The GFET N_j is, thus, the main contribution to the overall noise figure in our setup (with pre-amplifier NSD $\sim 7\ \text{nV}\ \text{Hz}^{-1/2}$). The measured NSD at 1.333 kHz is then used to calculate NEP [Figs. 3(d) and 3(e)] as a function of the voltages applied to the gate electrodes.

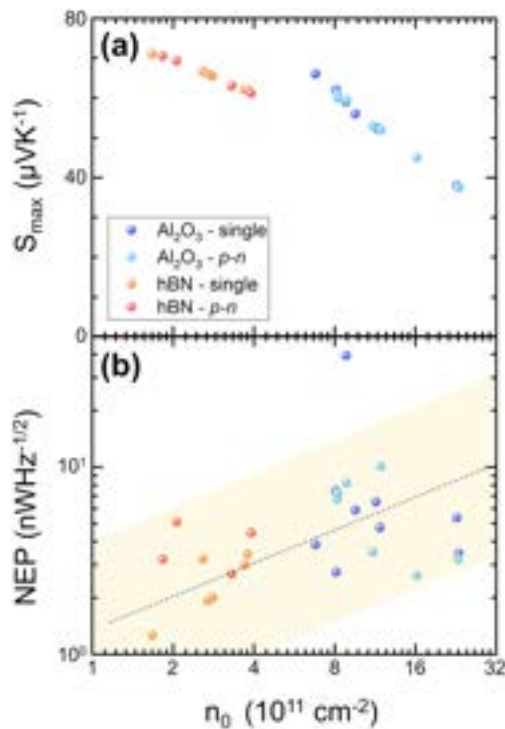


FIG. 4. (a) Scatterplot of S_{\max} vs n_0 . Differently colored dots identify different material/geometry combinations. S_{\max} and n_0 have negative correlation. (b) NEP vs n_0 chart, showing positive correlation: $\rho[\log(\text{NEP}), \log(n_0)] = 0.4$. The dotted line is a guide for the eye.

We then characterize the detection speed by recording the time trace of Δu with an oscilloscope (Tektronix DPO520-4B, bandwidth 2 GHz). We use a THz pulse duration $\sim 1.6 \mu\text{s}$, and we amplify the PD output with a high-bandwidth (1.1 GHz) voltage preamplifier (Femto, DUPVA-1-70) before the oscilloscope. We drive the QCL into the negative differential resistance regime,³⁰ which results in electronic instabilities that correspond to an intermittent output power: the QCL undergoes intensity fluctuations with characteristic time constants $\tau_{\text{qcl}} \sim 0.9 \text{ ns}$. This strategy allows us to test the bandwidth of our PDs up to a maximum $(2\pi\tau_{\text{qcl}})^{-1} = 180 \text{ MHz}$. Figure 3(f) shows the waveform recorded by a single-gated GFET during an intensity fluctuation of the pulsed QCL. We evaluate τ from exponential fits to the waveform (see the supplementary material). We get $\tau = 7\text{--}20 \text{ ns}$ for the investigated devices, with a mean value $\sim 12 \text{ ns}$, corresponding to a bandwidth $\sim 15 \text{ MHz}$.

Statistical analysis is applied to 28 devices to evaluate performance variability and identify correlations between electrical and optical properties. We first consider NEP variability. For $\text{Al}_2\text{O}_3/\text{SLG}/\text{HfO}_2$ devices, we get a mean value $\sim 7.6 \text{ nW Hz}^{-1/2}$ and an interquartile range²⁸ (IQR) $\sim 4.0 \text{ nW Hz}^{-1/2}$. For hBN-capped PDs, we have mean NEP $\sim 3.0 \text{ nW Hz}^{-1/2}$ with IQR $\sim 1.4 \text{ nW Hz}^{-1/2}$, which represents a variability improvement of factor >2 with respect to SiO_2/SLG ²⁴ and $\text{Al}_2\text{O}_3/\text{SLG}$ PDs. We then evaluate correlations among NEP, S_b , and n_0 using the Pearson coefficient⁶⁰ (ρ) as a metric. $\rho(v_1, v_2)$ represents the measure of linear correlation between two discrete variables v_1 and v_2 : $|\rho| = 1$ indicates an exact linear dependence and $\rho = 0$ indicates no

linear correlation. We get $\rho(S_{\max}, n_0) = -0.95$ for both hBN-capped and uncapped architectures, where S_{\max} is the maximum $|S_b|$ in the investigated V_g range, calculated with the EMT model. The scatterplot of S_{\max} vs n_0 in Fig. 4(a) shows that hBN/SLG/ Al_2O_3 LMHs have slightly larger S_{\max} , even though they have significantly smaller n_0 . This is due to the different dielectric environment: the larger ϵ_r of HfO_2 (with respect to hBN) on top of SLG is beneficial in terms of thermopower.⁵⁶ This similarity in S_{\max} is reflected in the detectors NEP, where the difference between the two material architectures is not as pronounced as the difference in n_0 [Fig. 4(b)]. However, in agreement with results obtained on $\text{SiO}_2/\text{SLG}/\text{HfO}_2$ heterostructures,²⁸ NEP increases for larger n_0 : $\rho[\log(\text{NEP}), \log(n_0)] = 0.4$. These correlations confirm that the physical mechanism underpinning THz detection is, as expected, PTE.

Thus, the Al_2O_3 termination alone does not show a significant performance improvement over SiO_2/Si substrates,²⁸ whereas large-area $\text{HfO}_2/\text{hBN}/\text{SLG}/\text{Al}_2\text{O}_3$ LMHs present advantages both in terms of absolute optical performance (average NEP $\sim 3.0 \text{ nW Hz}^{-1/2}$) and performance variability (IQR $\sim 1.40 \text{ nW Hz}^{-1/2}$). Large area hBN-top-encapsulation significantly reduces the device performance variability by over a factor 2 with respect to Ref. 28.

In summary, we reported THz PDs realized with large-area graphene and large-area hBN in wafer-scale compliant processes, capable of mitigating material degradation with respect to the quality benchmark of hBN-encapsulated SLG.²⁹⁻³¹ We demonstrate THz detection in a layered material heterostructure obtained by consecutive transfer of CVD graphene and CVD hexagonal boron nitride, a fabrication technique compatible with CMOS processing. This makes our PDs suitable for real-time imaging and short-range ($\sim 10 \text{ m}$) THz communication applications, enabling multi-pixel architectures. A further benefit can come from the full large-area encapsulation of SLG in CVD-based hBN/SLG/hBN heterostructures.

See the supplementary material for the description of Al_2O_3 ALD, thermopower calculation, and detection speed analysis.

We acknowledge funding from ERC Projects via No. 681379 (SPRINT), Hetero2D, GSYNCOR, the EU Graphene and Quantum Flagships, the Marie Curie H2020-MSCA-ITN2017 TeraApps (No. 765426) grant, the CNR project (TEROCODE), EPSRC Grant Nos. EP/L016087/1, EP/K01711X/1, EP/K017144/1, EP/N010345/1, EP/V000055/1, and DSTL, University of Pisa under the ‘‘PRA-Progetti di Ricerca di Ateneo’’ (Institutional Research Grants)—Project No. PRA 2020-2021 92. For the purpose of open access, the authors applied a Creative Commons Attribution (CC BY) license to any Author Accepted Manuscript version arising from this submission.

AUTHOR DECLARATIONS

Conflict of Interest

The authors have no conflicts to disclose.

Author Contributions

Mahdi Asgari: Investigation (lead). **Clifford McAleese:** Investigation (supporting). **Ben Conran:** Investigation (supporting). **Xiaochen Wang:** Investigation (supporting). **Andrea Tomadin:** Formal analysis (supporting). **Andrea C. Ferrari:**

Resources (supporting), Writing – review and editing (supporting). **Miriam Serena Vitiello**: Conceptualization (Lead); Methodology (equal); Supervision (Lead); Writing – review and editing (equal), Resources (Lead). **Leonardo Viti**: Investigation (supporting); Methodology (equal); Formal analysis (equal); Writing – original draft (Lead). **Osman Balci**: Investigation (supporting). **Sachin Shinde**: Investigation (equal). **Jincan Zhang**: Investigation (supporting). **Hamideh Ramezani**: Investigation (supporting). **Subash Sharma**: Investigation (supporting). **Adil Meersha**: Investigation (supporting). **Guido Menichetti**: Formal analysis (equal).

DATA AVAILABILITY

The data that support the findings of this study are available from the corresponding author upon reasonable request.

REFERENCES

- F. Bonaccorso, Z. Sun, T. Hasan, and A. C. Ferrari, *Nat. Photonics* **4**, 611 (2010).
- A. C. Ferrari, F. Bonaccorso, V. Fal'ko, K. S. Novoselov, S. Roche, P. Bøggild, S. Borini, F. H. L. Koppens, V. Palermo, N. Pugno, J. A. Garrido, R. Sordan, A. Bianco, L. Ballerini, M. Prato, E. Lidorikis, J. Kivioja, C. Marinelli, T. Ryhänen, A. Morpurgo, J. N. Coleman, V. Nicolosi, L. Colombo, A. Fert, M. Garcia-Hernandez, A. Bachtold, G. F. Schneider, F. Guinea, C. Dekker, M. Barbone, Z. Sun, C. Galiotis, A. N. Grigorenko, G. Konstantatos, A. Kis, M. Katsnelson, L. Vandersypen, A. Loiseau, V. Morandi, D. Neumaier, E. Treossi, V. Pellegrini, M. Polini, A. Tredicucci, G. M. Williams, B. Hee Hong, J.-H. Ahn, J. Min Kim, H. Zirath, B. J. van Wees, H. van der Zant, L. Occhipinti, A. Di Matteo, I. A. Kinloch, T. Seyller, E. Quesnel, X. Feng, K. Teo, N. Rupasinghe, P. Hakonen, S. R. T. Neil, Q. Tannock, T. Löfwander, and J. Kinaret, *Nanoscale* **7**, 4598–4810 (2015).
- F. H. L. Koppens, T. Mueller, P. Avouris, A. C. Ferrari, M. S. Vitiello, and M. Polini, *Nat. Nanotechnol.* **9**, 780 (2014).
- F. Bonaccorso, A. Lombardo, T. Hasan, Z. Sun, L. Colombo, and A. C. Ferrari, *Mater. Today* **15**, 564 (2012).
- C. Backes, A. M. Abdelkader, C. Alonso, A. Andrieux-Ledier, R. Arenal, J. Azpeitia, N. Balakrishnan, L. Banszerus, J. Barjon, R. Bartali, S. Bellani, C. Berger, R. Berger, M. M. Bernal Ortega, C. Bernard, P. H. Beton, A. Beyer, A. Bianco, P. Bøggild, F. Bonaccorso, G. Borin Barin, C. Botas, R. A. Bueno, D. Carriazo, A. Castellanos-Gomez, M. Christian, A. Ciesielski, T. Ciuk, M. T. Cole, J. Coleman, C. Coletti, L. Crema, H. Cun, D. Dasler, D. De Fazio, N. Díez, S. Drieschner, G. S. Duesberg, R. Fasel, X. Feng, A. Fina, S. Forti, C. Galiotis, G. Garberoglio, J. M. García, J. A. Garrido, M. Gibertini, A. Götzhäuser, J. Gómez, T. Greber, F. Hauke, A. Hemmi, I. Hernandez-Rodriguez, A. Hirsch, S. A. Hodge, Y. Huttel, P. U. Jepsen, I. Jimenez, U. Kaiser, T. Kaplas, H. K. Kim, A. Kis, K. Papagelis, K. Kostarelos, A. Krajewska, K. Lee, C. Li, H. Lipsanen, A. Liscio, M. R. Lohe, A. Loiseau, L. Lombardi, M. F. López, O. Martín, C. Martín, L. Martínez, J. A. Martín-Gago, J. I. Martínez, N. Marzari, Á. Mayoral, J. McManus, M. Melucci, J. Méndez, C. Merino, P. Merino, A. P. Meyer, E. Miniussi, V. Miseikis, N. Mishra, V. Morandi, C. Munuera, R. Muñoz, H. Nolan, L. Ortolani, A. K. Ott, I. Palacio, V. Palermo, J. Parthenios, I. Pasternak, A. Patane, M. Prato, H. Prevost, V. Prudkovskiy, N. Pugno, T. Rojo, A. Rossi, P. Ruffieux, P. Samori, L. Schué, E. Setijadi, T. Seyller, G. Speranza, C. Stampfer, I. Stenger, W. Strupinski, Y. Svirko, S. Taioli, K. B. K. Teo, M. Testi, F. Tomarchio, M. Tortello, E. Treossi, A. Turchanin, E. Vazquez, E. Villaro, P. R. Whelan, Z. Xia, R. Yakimov, S. Yang, G. R. Yazdi, C. Yim, D. Yoon, X. Zhang, X. Zhuang, L. Colombo, A. C. Ferrari, and M. Garcia-Hernandez, *2D Mater.* **7**, 022001 (2020).
- M. Romagnoli, V. Soriano, M. Midrio, F. H. L. Koppens, C. Huyghebaert, D. Neumaier, P. Galli, W. Templ, A. D'Errico, and A. C. Ferrari, *Nat. Rev. Mater.* **3**, 392 (2018).
- D. Akinwande, C. Huyghebaert, C.-H. Wang, M. I. Serna, S. Goossens, L.-J. Li, H.-S. P. Wong, and F. H. L. Koppens, *Nature* **573**, 507 (2019).
- V. Miseikis, S. Marconi, M. A. Giambra, A. Montanaro, L. Martini, F. Fabbri, S. Pezzini, G. Piccinini, S. Forti, B. Terres, I. Goykhman, L. Hamidouche, P. Legagneux, V. Soriano, A. C. Ferrari, F. H. L. Koppens, M. Romagnoli, and C. Coletti, *ACS Nano* **14**, 11190 (2020).
- A. Reserbat-Plantey, I. Epstein, I. Torre, A. T. Costa, P. A. D. Gonçalves, N. A. Mortensen, M. Polini, J. C. W. Song, N. M. R. Peres, and F. H. L. Koppens, *ACS Photonics* **8**, 85–101 (2021).
- M. Saeed, P. Palacios, M.-D. Wei, E. Baskent, C.-Y. Fan, B. Uzlu, K.-T. Wang, A. Hemmetter, Z. Wang, D. Neumaier, M. C. Lemme, and R. Negra, *Adv. Mater.* **2022**, 2108473.
- A. Glushkova, P. Andričević, R. Smajda, B. Náfrádi, M. Kollár, V. Djokić, A. Arakcheeva, L. Forró, R. Pugin, and E. Horváth, *ACS Nano* **15**, 4077 (2021).
- M. Tonouchi, *Nat. Photonics* **1**, 97–105 (2007).
- S. S. Dhillon, M. S. Vitiello, E. H. Linfield, A. G. Davies, M. C. Hoffmann, J. Booske, C. Paoloni, M. Gensch, P. Weightman, G. P. Williams, E. Castro-Camus, D. R. S. Cumming, F. Simoens, I. Escorcia-Carranza, J. Grant, S. Lucyszyn, M. Kuwata-Gonokami, K. Konishi, M. Koch, C. A. Schmuttenmaer, T. L. Cocker, R. Huber, A. G. Markelz, Z. D. Taylor, V. P. Wallace, J. A. Zeitler, J. Sibik, T. M. Korter, B. Ellison, S. Rea, P. Goldsmith, K. B. Cooper, R. Appleby, D. Pardo, P. G. Huggard, V. Krozer, H. Shams, M. Fice, C. Renaud, A. Seeds, A. Stöhr, M. Naftaly, N. Ridler, R. Clarke, J. E. Cunningham, and M. B. Johnston, *J. Phys. D* **50**, 043001 (2017).
- N. Nagai, R. Kumazawa, and R. Fukasawa, *Chem. Phys. Lett.* **413**, 495 (2005).
- A. Cosentino, *Technologies* **4**, 6 (2016).
- P. M. Echternach, B. J. Pepper, T. Reck, and C. M. Bradford, *Nat. Astron.* **2**, 90 (2018).
- R. I. Stantchev, X. Yu, T. Blu, and E. Pickwell-MacPherson, *Nat. Commun.* **11**, 2535 (2020).
- T. Nagatsuma, G. Ducournau, and C. C. Renaud, *Nat. Photonics* **10**, 371 (2016).
- B. Sensale-Rodriguez, R. Yan, M. M. Kelly, T. Fang, K. Tahy, W. S. Hwang, D. Jena, L. Liu, and H. G. Xing, *Nat. Commun.* **3**, 780 (2012).
- S. J. Kindness, N. W. Almond, W. Michailow, B. Wei, L. A. Jakob, K. Delfanazari, P. Braeuninger-Weimer, S. Hofmann, H. E. Beere, D. A. Ritchie, and R. Degl'Innocenti, *ACS Photonics* **6**, 1547 (2019).
- V. Bianchi, T. Carey, L. Viti, L. Li, E. H. Linfield, A. G. Davies, A. Tredicucci, D. Yoon, P. G. Karagiannidis, L. Lombardi, F. Tomarchio, A. C. Ferrari, F. Torrisi, and M. S. Vitiello, *Nat. Commun.* **8**, 15763 (2017).
- H. A. Hafez, S. Kovalev, J.-C. Deinert, Z. Mics, B. Green, N. Awari, M. Chen, S. Germanskiy, U. Lehnert, J. Teichert, Z. Wang, K.-J. Tielrooij, Z. Liu, Z. Chen, A. Narita, K. Müllen, M. Bonn, M. Gensch, and D. Turchinovic, *Nature* **561**, 507–511 (2018).
- F. Bianco, D. Perenzoni, D. Convertino, S. L. De Bonis, D. Spirito, D. M. Perenzoni, C. Coletti, M. S. Vitiello, and A. Tredicucci, *Appl. Phys. Lett.* **107**, 131104 (2015).
- F. Bianco, V. Miseikis, D. Perenzoni, C. Coletti, M. Perenzoni, and A. Tredicucci, *IEEE Trans. Terahertz Sci. Technol.* **11**, 70–78 (2021).
- A. A. Generalov, M. A. Andersson, X. Yang, A. Vorobiev, and J. Stake, *IEEE Trans. Terahertz Sci. Technol.* **7**, 614–616 (2017).
- A. Zak, M. A. Andersson, M. Bauer, J. Matukas, A. Lisauskas, H. G. Roskos, and J. Stake, *Nano Lett.* **14**, 5834 (2014).
- R. Degl'Innocenti, L. Xiao, D. S. Jessop, S. J. Kindness, Y. Ren, H. Lin, J. A. Zeitler, J. A. Alexander-Webber, H. J. Joyce, and P. Braeuninger-Weimer, *ACS Photonics* **3**, 1747–1753 (2016).
- M. Asgari, E. Riccardi, O. Balci, D. De Fazio, S. M. Shinde, J. Zhang, S. Mignuzzi, F. H. L. Koppens, A. C. Ferrari, L. Viti, and M. S. Vitiello, *ACS Nano* **15**, 17966 (2021).
- S. Castilla, B. Terrés, M. Autore, L. Viti, J. Li, A. Y. Nikitin, I. Vangelidis, K. Watanabe, T. Taniguchi, E. Lidorikis, M. S. Vitiello, R. Hillenbrand, K.-J. Tielrooij, and F. H. L. Koppens, *Nano Lett.* **19**, 2765 (2019).
- L. Viti, D. G. Purdie, A. Lombardo, A. C. Ferrari, and M. S. Vitiello, *Nano Lett.* **20**, 3169 (2020).
- L. Viti, A. R. Cadore, X. Yang, A. Vorobiev, J. E. Muench, K. Watanabe, T. Taniguchi, J. Stake, A. C. Ferrari, and M. S. Vitiello, *Nanophotonics* **10**, 89–98 (2020).
- D. A. Bandurin, I. Gayduchenko, Y. Cao, M. Moskotin, A. Principi, I. V. Grigorieva, G. Goltsman, G. Fedorov, and D. Svintsov, *Appl. Phys. Lett.* **112**, 141101 (2018).
- J. A. Delgado-Notario, W. Knap, V. Clericò, J. Salvador-Sánchez, J. Calvo-Gallego, T. Taniguchi, K. Watanabe, T. Otsuji, V. V. Popov, D. V. Fateev, E.

- Diez, J. E. Velázquez-Pérez, and Y. M. Meziani, *Nanophotonics* **11**, 519–529 (2022).
- ³⁴D. Yadav, S. Boubanga Tombet, T. Watanabe, S. Arnold, V. Ryzhii, and T. Otsuji, *2D Mater.* **3**, 045009 (2016).
- ³⁵See <http://www.vadiodes.com> for information about commercial Schottky diode detectors.
- ³⁶S. Regensburger, S. Winnerl, J. M. Klopff, H. Lu, A. C. Gossard, and S. Preu, *IEEE Trans. Terahertz Sci. Technol.* **9**, 262 (2019).
- ³⁷F. Simoens and J. Meilhan, *Philos. Trans. R. Soc., A* **372**, 20130111 (2014).
- ³⁸F. Sizov, *Semicond. Sci. Technol.* **33**, 123001 (2018).
- ³⁹H. Yang, S. Qin, X. Zheng, G. Wang, Y. Tan, G. Peng, and X. Zhang, *Nanomaterials* **7**, 286 (2017).
- ⁴⁰V. Shautsova, A. M. Gilbertson, N. C. G. Black, S. A. Maier, and L. F. Cohen, *Sci. Rep.* **6**, 30210 (2016).
- ⁴¹A. Das, S. Pisana, B. Chakraborty, S. Piscanec, S. K. Saha, U. V. Waghmare, K. S. Novoselov, H. R. Krishnamurthy, A. K. Geim, A. C. Ferrari, and A. K. Sood, *Nat. Nanotechnol.* **3**, 210 (2008).
- ⁴²D. M. Basko, S. Piscanec, and A. C. Ferrari, *Phys. Rev. B* **80**, 165413 (2009).
- ⁴³M. Bruna, A. K. Ott, M. Ijas, D. Yoon, U. Sassi, and A. C. Ferrari, *ACS Nano* **8**, 7432–7441 (2014).
- ⁴⁴A. A. Lagatsky, Z. Sun, T. S. Kulmala, R. S. Sundaram, S. Milana, F. Torrisi, O. L. Antipov, Y. Lee, J. H. Ahn, C. T. A. Brown, W. Sibbett, and A. C. Ferrari, *Appl. Phys. Lett.* **102**, 013113 (2013).
- ⁴⁵A. C. Ferrari, J. C. Meyer, V. Scardaci, C. Casiraghi, M. Lazzeri, F. Mauri, S. Piscanec, D. Jiang, K. S. Novoselov, S. Roth, and A. K. Geim, *Phys. Rev. Lett.* **97**, 187401 (2006).
- ⁴⁶A. C. Ferrari and J. Robertson, *Phys. Rev. B* **61**, 14095 (2000).
- ⁴⁷A. C. Ferrari and D. M. Basko, *Nat. Nanotechnol.* **8**, 235 (2013).
- ⁴⁸S. Reich, A. C. Ferrari, R. Arenal, A. Loiseau, I. Bello, and J. Robertson, *Phys. Rev. B* **71**, 205201 (2005).
- ⁴⁹M. Massicotte, G. Soavi, A. Principi, and K.-J. Tielrooij, *Nanoscale* **13**, 8376–8411 (2021).
- ⁵⁰E. Pop, V. Varshney, and A. K. Roy, *MRS Bull.* **37**, 1273–1281 (2012).
- ⁵¹D. Brida, A. Tomadin, C. Manzoni, Y. I. Kim, A. Lombardo, S. Milana, R. Nair, K. S. Novoselov, A. C. Ferrari, G. Cerullo, and M. Polini, *Nat. Commun.* **4**, 1987 (2013).
- ⁵²K.-J. Tielrooij, N. C. H. Hesp, A. Principi, M. B. Lundberg, E. A. A. Pogna, L. Banszerus, Z. Mics, M. Massicotte, P. Schmidt, D. Davydovskaya, D. G. Purdie, I. Goykhman, G. Soavi, A. Lombardo, K. Watanabe, T. Taniguchi, M. Bonn, D. Turchinovich, C. Stampfer, A. C. Ferrari, G. Cerullo, M. Polini, and F. H. L. Koppens, *Nat. Nanotechnol.* **13**, 41 (2018).
- ⁵³A. Tomadin, D. Brida, G. Cerullo, A. C. Ferrari, and M. Polini, *Phys. Rev. B* **88**, 035430 (2013).
- ⁵⁴S. Castilla, I. Vangelidis, V.-V. Pusapati, J. Goldstein, M. Autore, T. Slipchenko, K. Rajendran, S. Kim, K. Watanabe, T. Taniguchi, L. Martín-Moreno, D. Englund, K.-J. Tielrooij, R. Hillenbrand, E. Lidorikis, and F. H. L. Koppens, *Nat. Commun.* **11**, 4872 (2020).
- ⁵⁵S. Kim, J. Nah, I. Jo, D. Shahrjerdi, L. Colombo, Z. Yao, E. Tutuc, and S. K. Banerjee, *Appl. Phys. Lett.* **94**, 062107 (2009).
- ⁵⁶E. H. Hwang, E. Rossi, and S. D. Sarma, *Phys. Rev. B* **80**, 235415 (2009).
- ⁵⁷A. Tomadin and M. Polini, *Phys. Rev. B* **104**, 125443 (2021).
- ⁵⁸See <http://zhinst.com> for information about the employed lock-in amplifier (model UHFLLI).
- ⁵⁹A. A. Balandin, *Nat. Nanotechnol.* **8**, 549–555 (2013).
- ⁶⁰A. G. Asuero, A. Sayago, and A. G. González, *Crit. Rev. Anal. Chem.* **36**, 41–59 (2006).